J. Fluid Mech. (2025), *vol.* 1018, A17, doi:10.1017/jfm.2025.10498

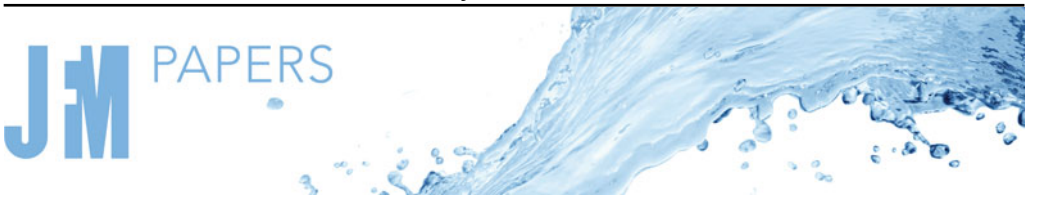

Lagrangian study of particle saltation in a turbulent boundary layer

Bernhard Roth[1], **Alec Petersen**[2], **Claudio Mucignat**[3] and **Filippo Coletti**[1]

[1]ETH Zurich, Department of Mechanical and Process Engineering, Zurich, Switzerland

[2]UC Irvine, University of California Irvine, Civil & Environmental Engineering, Irvine, CA, USA

[3]Empa, Swiss Federal Laboratories for Materials Science and Technology, Laboratory of Multiscale Studies in Building Physics, Dübendorf, Switzerland

Corresponding author: Bernhard Roth, rothbe@ethz.ch

(Received 16 January 2025; revised 13 June 2025; accepted 18 July 2025)

We study aeolian saltation over an erodible bed at full transport capacity in a wind tunnel with a relatively thick boundary layer. Lagrangian tracking of size-selected spherical particles resolves their concentration, velocity and acceleration. The mean particle concentration follows an exponential profile, while the mean particle velocity exhibits a convex shape. In contrast to current assumptions, both quantities appear sensitive to the friction velocity. The distributions of horizontal accelerations are positively skewed, though they contain negative tails associated with particles travelling faster than the fluid. The mean wind velocity profiles, reconstructed down to millimetric distances from the bed using the particle equation of motion, have an approximately constant logarithmic slope and do not show a focal point. The aerodynamic drag force increases with distance from the wall and, for the upward moving particles, exceeds the gravity force already at a few particle diameters from the bed. The vertical drag component resists the motion of both upward and downward moving particles with a magnitude comparable to the lift force, which is much smaller than gravity but non-negligible. Coupling the assumption of ballistic vertical motion and the measured streamwise velocities, the mean trajectories are reconstructed and found to be strongly influenced by aerodynamic drag. This is also confirmed by the direct identification of trajectory apexes, and demonstrated over a wide range of friction velocities. Taken together, these results indicate that aerodynamic drag and lift may play a more significant role in the saltation process than presently recognized, being complementary rather than alternative to splash processes.

Key words: particle/fluid flow, sediment transport

1. Introduction

The transport of particles caused by fluid flowing over a mobile bed is a key process in engineering (Vowinckel 2021; Capecelatro 2022) as well as in the environment (Richter & Gill 2018; Ancey & Pascal 2020). In geophysical flows the transport is often non-suspended, i.e. the particles are in regular contact with the bed, since turbulent fluctuations are unable to support their weight (Pähtz & Durán 2020). Here we focus on aeolian saltation, in which solid particles (typically sand or snow) of diameter $d_p = 100{-}600\ \mu\mathrm{m}$ move in large ballistic hops in a transport layer of thickness $h \gg d_p$ (Kok *et al.* 2012) over an erodible bed. The inception of the process is usually termed fluid entrainment or aerodynamic entrainment, in which the wind lifts grains from the bed by applying a stress above a so-called fluid threshold. The grains are then accelerated by aerodynamic drag and transfer the gained momentum to the bed upon collision. Impacting particles rebound and/or eject other grains (a process often called impact entrainment or splash entrainment), increasing the load in the saltation layer and extracting momentum from the wind until an equilibrium is reached. Because the momentum transfer by bed collision is more efficient than by aerodynamic drag, the impact threshold, i.e. the minimum wind stress at which saltation can be sustained after inception, is lower than the fluid threshold.

While this general picture was essentially defined already in the seminal works of Bagnold (1941) and Owen (1964), several crucial aspects remain poorly understood, causing key quantities (notably the mass flux) to be insufficiently constrained in present models of sand and snow transport (Clifton, Rüedi & Lehning 2006; Zheng 2009; Martin & Kok 2018). As such, they remain an object of intense debate. Because the topic is vast and has been reviewed in detail (Nickling & Neuman 2009; Zheng 2009; Claudin, Charru & Andreotti 2011; Kok *et al.* 2012; Valance *et al.* 2015; Pähtz *et al.* 2020), here we focus on selected aspects specifically relevant to the present study. While here we are concerned with solid particles, several of those aspects are also crucial to snow saltation, as comprehensively reviewed in Melo, Sigmund & Lehning (2024). A key issue is the relative importance of fluid entrainment and impact entrainment, which traces back to Owen (1964). He argued that, in equilibrium, the fluid stress on the bed surface equates the impact threshold: a lower surface stress would result in fewer entrained particles, reducing the momentum extracted from the wind and increasing the surface stress back to the threshold; while the opposite would happen if the surface stress were higher than the threshold. This self-regulating mechanism is at the basis of simple models of sediment erosion (Raupach 1991; Doorschot & Lehning 2002; Kok & Renno 2009) but assumes that fluid entrainment dominates over impact entrainment. This is inconsistent with the occurrence of saltation below the fluid threshold as already documented by Bagnold (1941). Moreover, only saltation models that assume impact-dominated entrainment can reproduce a 'focus' in the near-bed wind profiles for different wind speeds, originally reported by Bagnold (1938).

The dominance of impact entrainment over fluid entrainment implies that particles failing to rebound are replaced by newly ejected ones, an equilibrium determined by a ballistic impact speed $O(\sqrt{\mathrm{g}d_p})$, where g is the gravitational acceleration (Beladjine *et al.* 2007; Kok & Renno 2009). Therefore, the particle speed too should be independent of u^* in the saltation layer, which is then identified as the region below the Bagnold focus (Durán *et al.* 2012; Valance *et al.* 2015; Melo *et al.* 2022). Other important consequences of this view are that the height of the saltator trajectories (related to the thickness of the saltation layer) as well as their length should be also independent of u^* (Sato, Kosugi & Sato 2004; Ho *et al.* 2011), and that the mass flux should scale linearly with the excess stress above the saltation threshold (Kok *et al.* 2012; Martin & Kok 2017). The evidence of impact-dominated entrainment is strong (Durán *et al.* 2012; Pähtz & Durán 2017;

Pähtz & Durán 2020) and several studies have reported results that support it, including the weak influence of the friction velocity on the thickness of the saltation layer and on the particle velocity within it (Creyssels *et al.* 2009; Ho *et al.* 2011; Martin & Kok 2017). Some experiments, however, have provided some support to Owen's hypothesis. Using laser Doppler anemometry, Li & Neuman (2012) measured fluid stress profiles converging towards the impact threshold as the surface is approached, as predicted by Owen. Walter *et al.* (2014) used an Irwin sensor to directly measure the wall shear stress, which decreased weakly with wind velocity at small and intermediate particle mass fluxes but remained essentially constant for high particle mass fluxes, again in agreement with Owen's hypothesis. They concluded that, while splashing is a more efficient way of transferring momentum to the surface particles than fluid drag, both should be considered as complementary entrainment processes.

Our understanding of the process is thwarted by the difficulty of achieving appropriate conditions for wind tunnel experiments, and measuring wind velocity and particle transport within the saltation layer (Rasmussen, Valance & Merrison 2015). Reaching equilibrium between the boundary layer flow and the saltation cloud typically requires particle beds $\approx$6 m or longer (Rasmussen *et al.* 2015) with a depth of centimetres to remain in the transport-limited regime (Li & Neuman 2012). The boundary layer thickness should also be sufficiently thick to allow for the development of a logarithmic profile. This is required for establishing the vertical momentum flux above the saltation layer, which is then partitioned between the airborne stress and the particle-borne stress (Raupach 1991; Li & Neuman 2012), and in turn to reliably measure u^* (Rasmussen, Iversen & Rautahemio 1996; Bauer, Houser & Nickling 2004). Moreover, as discussed in detail by Bauer *et al.* (2004), the limited cross-section of typical wind tunnel studies imposes an artificial over-steepening to the wind velocity profile. From the metrological standpoint, the saltation layer is a harsh environment for physical probes, and its optical thickness challenges non-intrusive measurements. Indeed, reported profiles of particle velocity and concentration typically contain fewer than 10 points in the wall-normal directions, making it hard to distinguish precise trends (Rasmussen *et al.* 2015). Obtaining a range of friction velocities wide enough to observe clear trends is also a challenge: the high transport rates mobilize large amounts of material, which may be complicated to handle in a laboratory setting. Recently, Ralaiarisoa *et al.* (2020) reported on transport rates and characteristic heights of the saltation layer for an unprecedented range of friction velocities and of its non-dimensional form, the Shields number (*Sh*, to be defined below). They concluded that the classic saltation regime at low and moderate *Sh* transitions to a collisional regime at higher *Sh*. This is characterized by frequent midair interparticle collisions, which have strong dispersive effects (Carneiro *et al.* 2013) and as such produce a growth of the transport layer.

Particle imaging and tracking has become the *de facto* standard to simultaneously obtain velocity and concentration at different distances from the bed (Creyssels *et al.* 2009; Ho *et al.* 2014; O'Brien & Neuman 2019). However, the basic shapes of the mean profiles differ significantly across the various studies. Moreover, while those Eulerian quantities provide important characterization, Lagrangian particle trajectories are most suitable to evaluate the forces acting on saltating particles, notably drag and lift. The seminal study of White & Schulz (1977) used high-speed photography to obtain saltating particles' trajectories, from which the authors evaluated the importance of the Magnus-lift due to particle rotation, later supported by the theoretical model of Huang, Wang & Pan (2010). Zou *et al.* (2007) used high-speed imaging to estimate the particle rotation rate and estimated its contribution to saltation height and length. Previous measurements, however, have not achieved sufficient temporal resolution to obtain particle acceleration, which is essential to directly evaluate the forces at play.

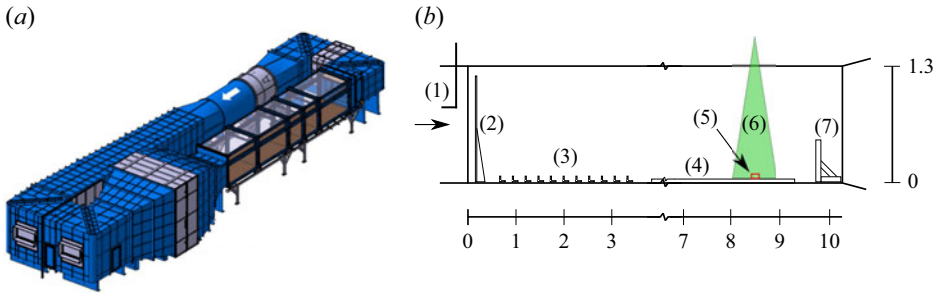

Figure 1. Overview drawing (*a*) and test section schematic (*b*) of the atmospheric wind tunnel used in the present study. The schematic depicts the position of the Pitot-tube (1), the turbulence spires (2), the roughness elements (3), the sand bed boundaries (4), the high-speed camera field of view (5), the laser sheet (6) and the filter frame (7). The axis are in units of metres.

As clear from the above, several outstanding questions remain, including: How do particle velocity and concentration evolve within the saltation layer? How do saltation height, length and velocity vary with friction velocity? What is the relative magnitude of the forces acting on the particles? With those questions in mind, here we present and analyse the results of a measurement campaign in which laser imaging is used to characterize the particle concentration, velocity and acceleration of saltating particles in an atmospheric wind tunnel. The size of the facility and the high spatial and temporal resolution of the measurements allow us to tackle some of the experimental challenges mentioned above. The data is used together with an analytical force model to reconstruct the wind speed at close distances from the bed, and to calculate the forces acting on the particles. Moreover, energetic arguments are used to model the mean particle trajectories. The paper is organized as follows. The experimental methodology and the considered regimes are described in § 2; the results are presented in § 3 in terms of particle concentration and kinematics (§ 3.1), force balance (§ 3.3) and saltation trajectories (§ 3.3); in § 4, the trend of the saltation height is presented over a wide range of friction velocities; § 4 includes a discussion and draws the main conclusions.

2. Methods and regimes

Experiments are conducted in the atmospheric wind tunnel at the Swiss Federal Laboratories for Materials Science and Technology (Dübendorf, Switzerland), as depicted in figure 1(*a*). This is a recirculating facility powered by a 110 kW fan, featuring a 5.7 : 1 contraction followed by a 10.5 m long straight test section. The cross-section is 1.9 m wide and 1.3 m high, with an adjustable roof that ensures negligibly small streamwise pressure gradient. The inflow is conditioned by a staggered array of 5 cm tall L-shaped roughness elements over the first 3.5 m of the floor, promoting the growth of the boundary layer (figure 1*b*). For the majority of the presented results, the roughness elements are preceded by 1.1-m tall spires at the entry of the test section. The roughness elements are followed by a 6 m long and 2 cm deep bed of spherical glass particles.

The particles consist of size-selected soda lime glass beads (Mo-Sci Corp.) of density $\rho_p = 2500\,\mathrm{kg\,m^{-3}}$, as shown in figure 2(*a*). Optical microscopy over 928 particles yields the size distribution in figure 2(*b*), with a mean $\pm$ standard deviation $d_p = 219 \pm 23\,\mu\mathrm{m}$, a median of 223 μm and sphericity above 0.9. Using the measured relative velocity with respect to the air and standard drag correlations (Clift, Grace & Weber 2005), the aerodynamic response time of the particles is estimated as $\tau_p = 163$ ms and their terminal

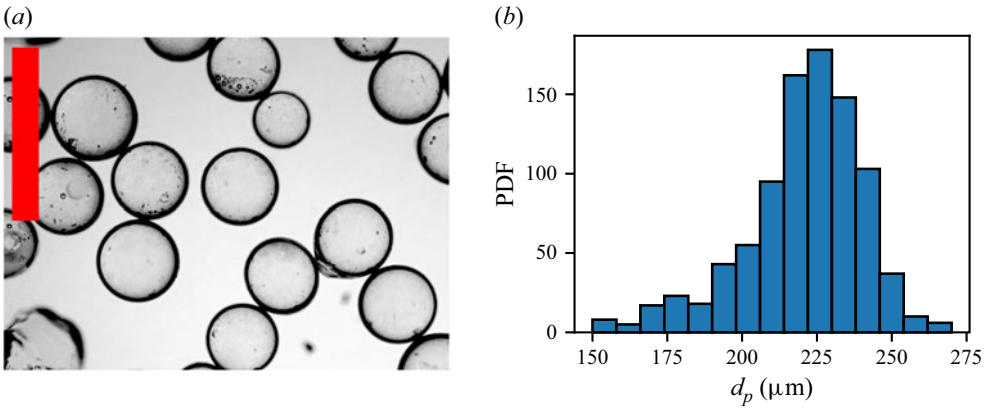

Figure 2. (*a*) Microscopic image of soda-lime glass particles used in this study. The red scale bar has a length of 500 μm. The corresponding particle diameter distribution (*b*), containing 928 samples, yields a mean diameter of 219 μm.

velocity in still air is $\tau_p g = 1.6\,\mathrm{m\,s^{-1}}$, using the particle relative velocity obtained from the measurements and the fluid velocity reconstruction as discussed in § 3.2. To limit the number of particles employed and their spreading in the test section, the bed is 0.6 m wide and confined by wooden plates that extend to the sidewalls of the test section. Additional measurements in which the bed is 0.25 m wide return statistically indistinguishable results. To prevent particles from recirculating through the tunnel, a 0.3 m tall filter with an 80 μm wire mesh is secured on the floor at the outlet of the test section.

To initiate the saltation process, the velocity measured by the Pitot tube is increased above the target level for around 10 s, and then reduced to the desired set point. This ensures reaching full transport capacity, i.e. the maximum transport the airflow can sustain without net particle accumulation on the bed (Pähtz *et al.* 2020). Each measurement run lasts approximately 5 min, before ripples begin to form (Andreotti, Claudin & Pouliquen 2006). Prior to every run, the bed is replenished and flattened, avoiding compaction effects which may change the saltation threshold and transport rates (Pähtz *et al.* 2020). Three incoming wind velocities (measured via a Pitot tube at the test section inlet), range between $U_{in} = 8$ and 10 m s^{-1}, well above the saltation threshold which is visually assessed around 6 m s^{-1}. Inspection of the image recordings confirms continuous saltation of the considered particles. The configuration without spires at the inlet results in smaller boundary layer thicknesses δ and higher u^*, as summarized in table 1, along with important parameters from selected previous studies of aeolian saltation. The relative humidity (RH) is monitored but not controlled. Two campaigns are carried out: one in which $RH = 50$ % and inlet spires are always present (whose results are presented in § 3), and one in which $RH = 20$ % and both configurations with and without spires are used (presented in § 4). The RH affects the cohesive interparticle forces and thus the quantitative saltation properties (McKenna Neuman & Sanderson 2008; Besnard *et al.* 2022), complicating the direct comparison between both campaigns (and in general comparisons across studies). This does not impact, however, the trends with friction velocity exhibited by both campaigns, as shown below.

The particle motion is imaged at a fetch of 5.5 m of erodible bed, using a Nd:YLF laser (Litron, 35 mJ pulse^{-1}) operated at 10 kHz and synchronized to a CMOS (complementary metal-oxide-semiconductor) camera (LaVision HS, 4 megapixel). The laser shines a 2-mm thick light sheet through the transparent ceiling of the test section, illuminating a

	d_p [μm]	Test section dimensions [m] (l, w, h)	δ [m]	u^* [m s^{-1}]	Sh [–]	Ga [–]	Re_τ [10^3]
Present study (20 % RH)	219	10, 1.9, 1.3	1.2	0.41	0.038	31	32
				0.53	0.063		42
				0.60	0.080		48
Present study (50 % RH)	219	10, 1.9, 1.3	0.6	0.29–2.6	0.018–1.5	31	12–104
Bauer *et al.* (2004)	190, 270	6.8, 0.9, 0.76	0.23–0.26	0.26–0.96	0.01–0.102	25–42	3.7–17
Rasmussen & Sørensen (2008)	242–320	15, 0.6, 0.9	0.14	0.27–0.74	0.01–0.11	36–55	2.5–6.9
Ho *et al.* (2011, 2014)	230, 630	6, 0.27, 0.27	–	0.35–1.00	0.02–0.21	33–151	–
Creyssels *et al.* (2009)	242	15, 0.6, 0.9	–	0.24–0.67	0.01–0.076	36	–
Li & Neuman (2012)	550	13.8, 0.7, 0.8	0.15	0.28–0.43	0.006–0.014	123	5.9–7.7
O'Brien & Neuman (2019)	590	13.5, 0.7, 0.8		0.33–0.62	0.008–0.028	137	–
Ralaiarisoa *et al.* (2020)	190	6, 0.27, 0.27	–	0.39–2.32	0.03–1.5	25	–
Martin & Kok (2017) (field data)	400–530	–	–	0.28–0.34	1.08–2.84	76–116	–

Table 1. Particle diameter d_p, test section length l, width w and height h, boundary layer thickness δ, friction velocity u^*, friction velocity u^*, Shields number Sh, Galileo number Ga and friction Reynolds number Re_τ of some recent wind tunnel studies of saltation. Field data from Martin & Kok (2017) is also reported here for reference. Here RH indicates the relative humidity of the air.

vertical streamwise plane at the test section midspan. The camera mounts a Nikon 200 mm lens at f/4.0, resulting in a field of view of 50 mm by 70 mm with a resolution of 24.1 pixels mm^{-1}. Perspective effects are minimized by centring the field of view at the bed surface, and by applying a pinhole model to a dot-pattern calibration target. The bed elevation is measured by detecting the reflection of the laser sheet on the sand bed as the point of maximum intensity in each column of the image. This information is used to correct the data during postprocessing, yielding a precision in the elevation coordinate of 0.5 mm or approximately two particle diameters.

The local particle volume fraction ϕ, in the range $O(10^{-5}-10^{-3})$, is evaluated via direct counting of the particles in the imaged volume (see Fong, Amili & Coletti 2019), where the approach was validated with a known particle mass loading (Hassaini & Coletti 2022; Hassaini, Petersen & Coletti 2023). The absolute value is affected by the uncertainty in evaluating the illuminated sheet thickness. This, however, does not affect the gradient of the wall-normal concentration profiles, on which our considerations will be based. The particle motion is evaluated by time-resolved particle tracking velocimetry (PTV) using an in-house code (Petersen, Baker & Coletti 2019), allowing us to reconstruct Lagrangian particle trajectories. The steps are similar as in previous studies in which particles in turbulent flows were tracked (e.g. Berk & Coletti 2021; Salmon *et al.* 2023) and are briefly summarized here. First, the background generated by a temporal moving minimum filter is subtracted, and low intensity out-of-focus particles are masked out. Particle centroids are detected with subpixel precision using a centre-of-mass algorithm and tracked using the fourth-best-estimate approach proposed by Ouellette, Xu & Bodenschatz (2006). The resulting trajectories are convolved with the first and second derivatives of a Gaussian kernel to obtain the particle velocities and acceleration, respectively, following the method

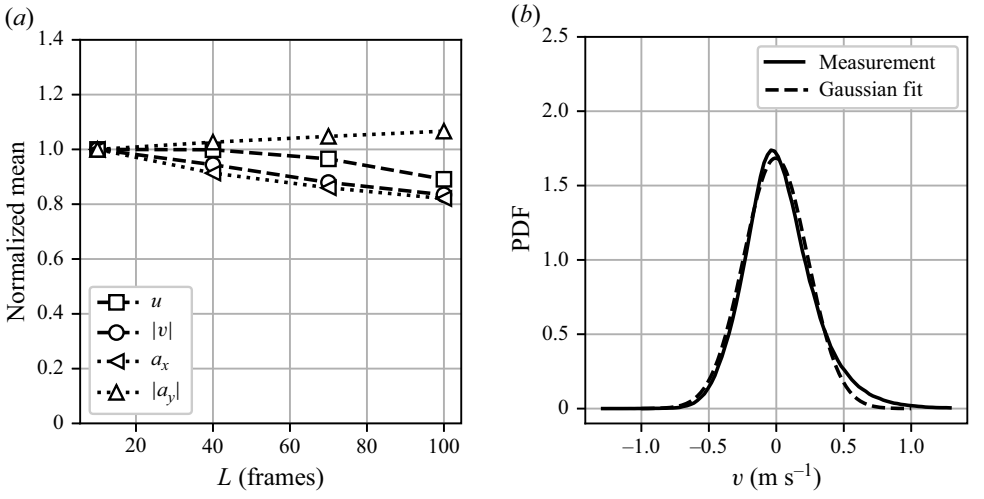

Figure 3. (*a*) Bias analysis using the normalized mean value, conditioned on the minimum trajectory length L. The bias is slightly more pronounced in the vertical direction, but remains well below 10 % at the trajectory length required for smoothing. (*b*) Typical vertical velocity distribution measured at $u^* = 0.53\ \mathrm{m\ s^{-1}}$.

proposed by Voth *et al.* (2002). A kernel width of 25 frames or 2.5 ms is used; as this is two orders of magnitude shorter than the particle response time, the convolution is not expected to filter out statistically significant features of the particle trajectories.

To ensure statistical convergence, 10 runs are carried out and ensemble-averaged for each case, yielding $O(10^7)$ detected particles and $O(10^6)$ trajectories. The high friction velocity in the configurations without spires leads to relatively large particle concentrations, which do not allow for accurate particle tracking. Thus, for those cases, we evaluate only the particle concentration profiles and the associated height of the saltation layer (see § 4).

The variance of the trajectory length is a well-known source of bias in the tracking process: because slower particles are likely to be tracked over longer trajectories, they could be over-represented in the statistics depending on the averaging operation (Mordant *et al.* 2004). To analyse the significance of such a bias in the present measurements, we consider the normalized mean particle velocity and acceleration, conditioned on the minimum trajectory length of 10 frames (figure 3*a*). The unconditional mean (i.e. the average over all trajectories irrespective of their length) is used for normalization. In the following, we denote with x the streamwise horizontal coordinate and with y the wall-normal vertical coordinate, the origin being located at the bed surface. We indicate as u and v the corresponding components of the particle velocity $\boldsymbol{u}$, while a_x, and a_y are the components of the particle acceleration $\boldsymbol{a}$. The bias appears to be more significant for the vertical components, while remaining below 10 % for the length required for smoothing. The mean vertical velocity is found to be negligibly small compared with its variance, as shown by the probability density function (PDF) in figure 3(*b*). This is consistent with the saltation process having reached equilibrium conditions at the measurement station. We note that the probability distribution of vertical velocities is approximately Gaussian (Creyssels *et al.* 2009; Durán *et al.* 2012), as discussed later.

The air flow in the boundary layer above the bed is characterized by particle image velocimetry (PIV) using 1–2 µm di-ethyl-hexyl-sebacate droplets as tracers, seeded in the flow before the contraction section using a Laskin nozzle. These are illuminated and imaged by the same system used for PTV. Figure 4(*a*) shows selected velocity

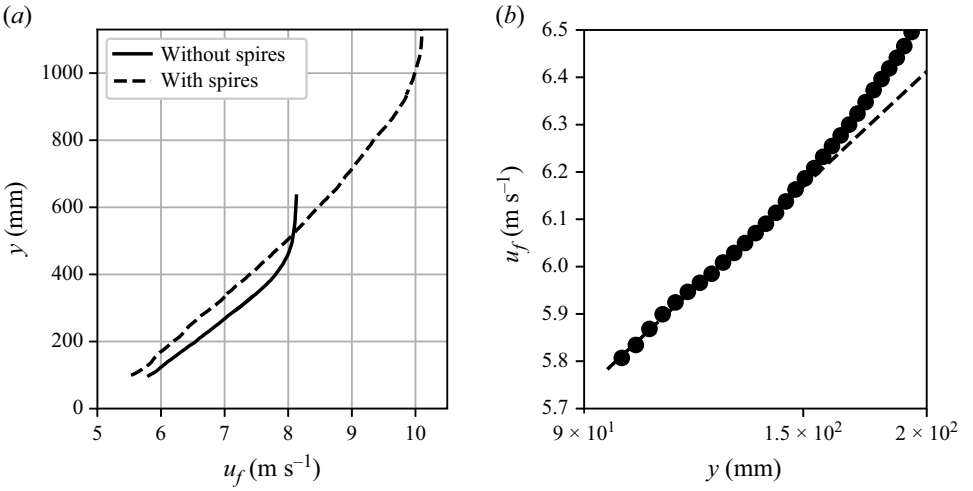

Figure 4. The PIV measurements of the horizontal fluid velocity profile with spires above the saltation layer for two sample cases with and without spires at the inlet of the test section. The comparison in linear scale in (*a*), between the configurations with and without spires at the inlet, show the significant difference in boundary layer thickness. Panel (*b*) shows the lower portion characteristic velocity profile with spires together with the logarithmic fit (dashed line) in the region below 150 mm, where the measured profile starts to deviate.

profiles, from the configuration with and without the spires at the inlet of the test section. Measurements are confined to the region 100 mm above the bed, due to the high effective optical density of the saltation layer and the reflectivity of the particle bed. They all display a logarithmic profile in the range 100 mm $<$ y $<$ 150 mm, as shown in figure 4(*b*), from which the friction velocity u^* in the classic law of the wall,

$$\langle u_f \rangle = \frac{u^*}{k} \ln \frac{y}{y_0}, \tag{2.1}$$

where u_f is the horizontal fluid velocity, $k = 0.41$ is the von Kármán constant and y_0 is the aerodynamic roughness. Here and in the following, angle brackets indicate temporal/ensemble averaging. A Clauser chart method (Clauser 1956 Wei, Schmidt & McMurtry 2005; Li & Neuman 2012), in which the logarithmic slope of the streamwise fluid velocity profile is compared with a canonical zero-pressure gradient turbulent boundary layer, is used to evaluate u^*. We define the Reynolds number $Re_\tau = u^*\delta\nu^{-1}$, the Shields number $Sh = \rho_f u^{*2}(\rho_p g d_p)^{-1}$ and the Galileo number $Ga = \sqrt{\rho_p - \rho_f} g d_p^3 (\rho_f \nu^2)^{-1}$, where ν and ρ_f are the air kinematic viscosity and density, respectively. The Shields number compares the aerodynamic and gravitational forces acting on the particles, while the Galileo number compares the gravitational and viscous forces. For the calculation of dimensionless numbers, a nominal kinematic viscosity of 1.5×10^{-5} m^2 s^{-1} is used. Though most parameters are within common ranges, Re_τ reaches significantly larger values compared with previous laboratory experiments owing to the relatively large cross-sectional size of the test section and the consequently thick boundary layer.

3. Results

The data is reported both in dimensional and non-dimensional form, using d_p, $\sqrt{g d_p}$ and g to normalize the length, velocity and acceleration, respectively. In §§ 3.1–3.3, we

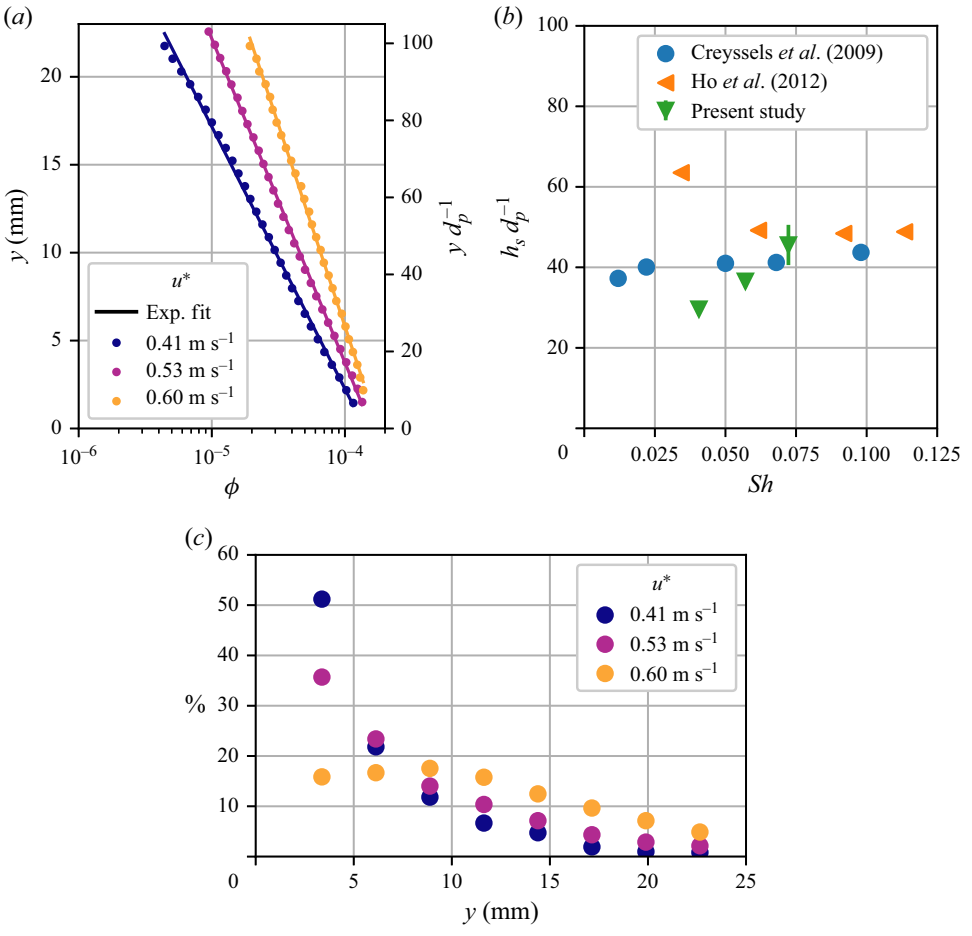

Figure 5. Panel (*a*) depicts the particle volume fraction profile for different friction velocities in semilogarithmic scale. The solid lines indicate the exponential fit. In addition to the expected increase of overall concentration with shear, an increase in decay height of the exponential profile is observed. Comparable wind-tunnel studies do not find a clear trend and propose a constant decay height, as shown in (*b*). Panel (*c*) shows the percentage of trajectories with apex at a given height, sampled from evenly spaced bins. The measurements indicate that the particles tend to have their apex at a height comparable to the decay height.

present the results of the first measurement campaign ($RH = 50$ %, with spires), including both particle motion and concentration. In § 4, we show the results of the concentration measurements obtained in the second campaign ($RH = 20$ %, with and without spires) which cover a much wider range of u^* and Sh.

3.1. *Particle concentration and kinematics*

The profiles of particle volume fraction are displayed in figure 5(*a*) for the three friction velocities. The semilogarithmic scale clearly highlights the exponential decay of the mean concentration $\langle c \rangle$, which closely follows the form

$$\langle c \rangle = c_0 \exp\left(\frac{-y}{h_s}\right), \tag{3.1}$$

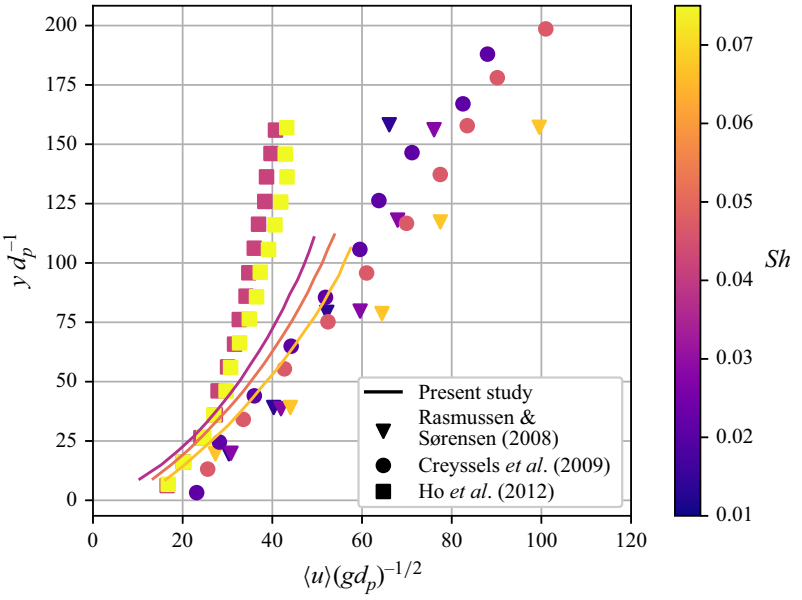

Figure 6. Comparison of the mean horizontal particle velocity profiles of different wind tunnel studies, spanning a similar range of Shields number.

where c_0 is a constant of units (m^{-3}), and h_s can be interpreted as the characteristic height of the saltation layer (Nalpanis, Hunt & Barrett 1993; Nishimura & Hunt 2000). The exponential fits yield $h_s = 6.5$, 8 and 10 mm for $u^* = 0.41$, 0.53 and 0.60 m s^{-1}, respectively. Given the large amount of data and large number of vertical bins compared with previous studies, the present results lend strong support to (3.1), as opposed to other functional dependencies (e.g. Dong *et al.* 2006; Zhang, Wang & Lee 2008). Assuming the particle motion in the vertical direction is ballistic (as confirmed in the following), the exponential decay of particle concentration implies a Gaussian distribution of vertical ejection velocities (Durán *et al.* 2012), see also figure 3(*b*). We do not observe the near-wall deviation from the exponential behaviour observed by Ho *et al.* (2012) which was attributed to a non-Gaussian velocity distribution of the saltating particles (Valance *et al.* 2015). Moreover, while the measured thickness of the saltation layer is compatible with the estimate $h_s \approx 40\,d_p$ by Creyssels *et al.* (2009), the observed increase of h_s with friction velocity is at odds with the view that h_s is independent from the friction velocity (Creyssels *et al.* 2009; Durán *et al.* 2012; Kok *et al.* 2012). This is quantitatively shown in figure 5(*b*), depicting the saltation height (normalized by the particle diameter) as a function of *Sh*, compared with those reported by Creyssels *et al.* (2009) and Ho *et al.* (2012). This trend is confirmed in figure 5(*c*), which presents the relative fraction of particles peaking at a given height of the particle trajectories that include both upward and downward phases: as the friction velocity increases, the probability distributions of the apex height shift to larger values. The magnitude of this shift is comparable to the increase in saltation decay height. It should be kept in mind, however, that the apexes of the saltating trajectories are only indirectly related to the concentration profile on which h_s is based on. Moreover, the distribution of the trajectory apexes is considered less robust than the concentration profiles, as the former requires capturing specific parts of each trajectory and not only the particle locations. Still, its trend corroborates the observation that the wind velocity influences the height of the saltation layer.

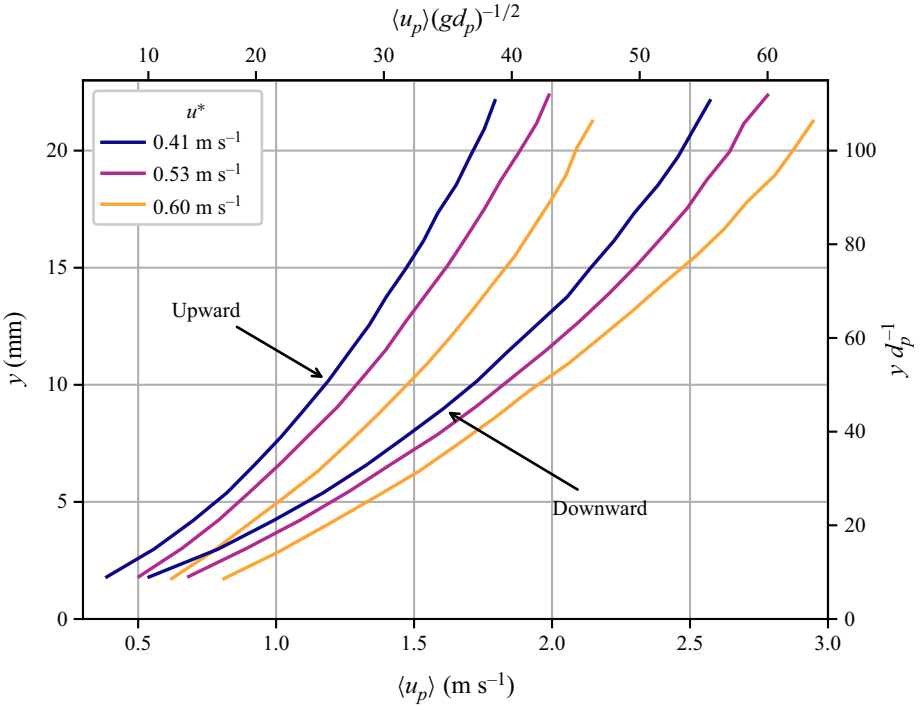

Figure 7. Mean horizontal particle velocity profiles, of separated upward- and downward-moving particle populations. The mean horizontal particle velocity is monotonically increasing with height and friction velocity for both populations, although their difference is increasing as the downward moving particles spent more time being accelerated by the air flow.

The horizontal particle velocity profiles are shown in figure 6. Besides the increase with friction velocity, the present measurements reveal a nonlinear dependency with wall-normal height. Rasmussen & Sørensen (2008) and Creyssels *et al.* (2009) reported logarithmic and linear trends, respectively, while Ho *et al.* (2012) reported a sharp change in slope inside the saltation layer. Our data, on the other hand, appears to follow a power law $\langle u \rangle \approx A y^b$ where $b \approx 1.8$, consistent with measurements by Liu & Dong (2004). In general, there is significant quantitative and qualitative disagreement between different experimental studies. Besides the shape of the profiles, the present results also denote a sizable increase of horizontal particle velocity with friction velocity. This is contrary to the independence of the particle velocity with u^*, which is assumed to follow from a purely impact-driven entrainment as discussed in the Introduction. It is consistent, however, with the increase in h_s reported above: due to the quasiballistic nature of saltator trajectories, h_s is expected to grow with the streamwise particle velocity (Owen 1964). Extrapolating the particle velocity to the bed location to determine a so-called slip velocity (i.e. the mean horizontal particle velocity at the bed surface) may lead to large uncertainties (Pähtz & Durán 2017). Therefore, while our data is as close to the bed as any previous study, we refrain from providing an estimated slip velocity (or ejection/impact velocities). However, the present data provides an upper bound $\approx 10\sqrt{g d_p}$ for the slip velocity in the considered range of parameters.

We now focus on the kinematics of the upward moving and downward moving particle populations, as their different behaviour is revealing of key aspects of saltation transport (Durán *et al.* 2012; Kok *et al.* 2012; Valance *et al.* 2015). Figure 7 presents profiles of

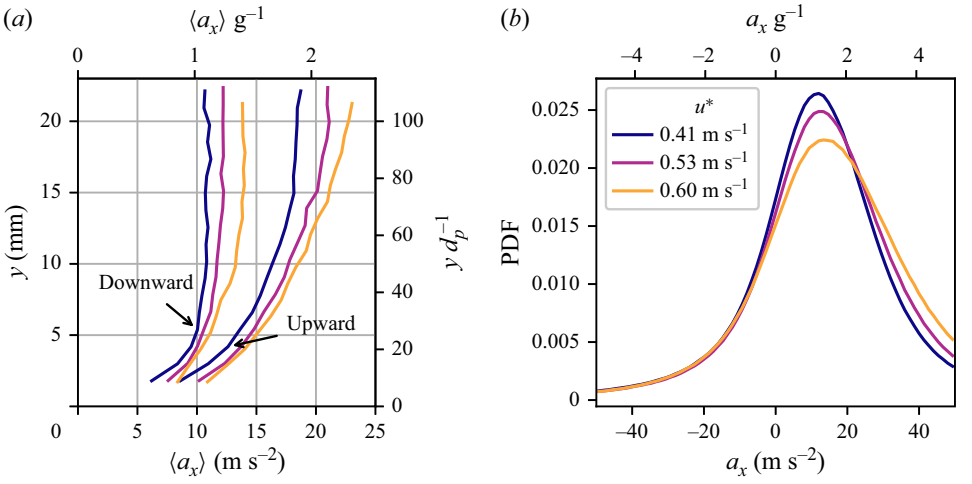

Figure 8. (*a*) Mean horizontal particle acceleration profiles of upward and downward moving particle populations. The legend of this panel is identical to the one given in (*b*). Both populations show a monotonous increase of acceleration with height and friction velocity. With increasing height, the change in acceleration reduces and reaches an almost constant value at the top of the saltation layer. (*b*) Horizontal particle acceleration distributions at different friction velocities. All three distributions are skewed towards higher accelerations. The width of the distributions and the length of the tail is increasing with increasing friction velocity.

mean horizontal velocities, showing that downward moving particles travel substantially faster, on average, than the upward moving particles. That is because the former have spent longer time being accelerated by the flow – an aspect we will expand upon in the following. The gap indeed grows with the distance from the bed, as the wind speed also grows. Both upward and downward populations show the same trend of increasing streamwise velocity with friction velocity.

The measurements of the acceleration components are especially useful in view of evaluating the forces acting on the particles. Figure 8(*a*) displays profiles of the mean horizontal acceleration, separating upward moving and downward moving particles. Because the former travel more slowly as shown above, they experience larger relative velocities with respect to the air flow and consequently larger drag, which implies higher streamwise accelerations. For both populations, the streamwise acceleration increases with increasing friction velocity throughout the saltation layer. As discussed, for example by Melo *et al.* (2024), the ratio $\langle a_x \rangle / g$ is proportional to the characteristic particle time of flight times the horizontal velocity difference between upward moving and downward moving particles. This quantity is expected to be independent of u^* for splash-dominated transport. This is in contrast with our observations, and rather in line with the increasing trends of particle concentration and velocity reported above. The PDFs of the horizontal acceleration (figure 8*b*) broaden with increasing friction velocity. Interestingly, a significant fraction of the particles experience a negative horizontal acceleration. This indicates they are travelling faster than the local wind, which imply they transfer momentum to the air. Such an exceptional scenario was hypothesized by Walter *et al.* (2014) to explain trends in their stress measurements at the bed. In general, the large width of the acceleration distribution (whose standard deviation is larger than its mean) is driven both by the variability of the particle saltating motion and by the turbulent airflow fluctuations.

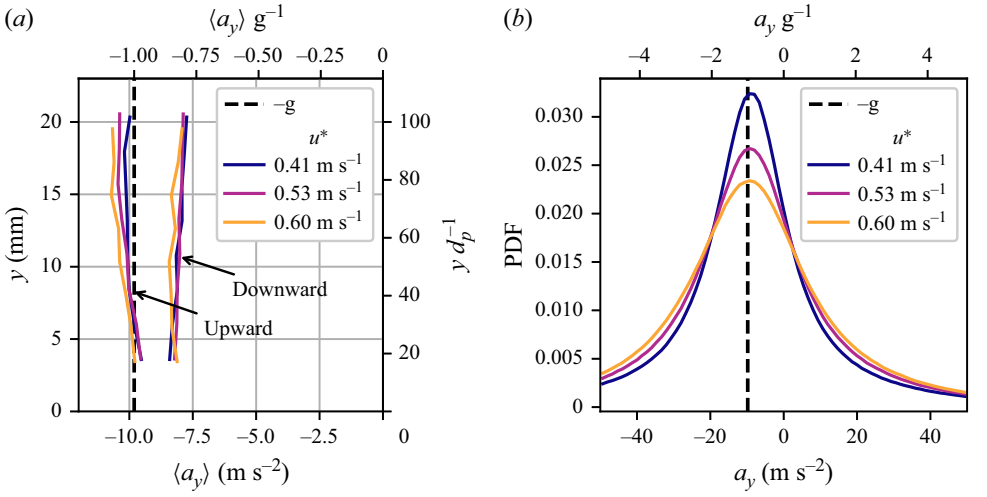

Figure 9. (*a*) Mean vertical particle acceleration profiles of upward and downward moving particle populations. The mean vertical acceleration is almost constant and weakly sensitive to friction velocity. The magnitude is close to the gravitational acceleration. A lift force causes a reduction in downwards acceleration and the different signs of the drag for upward and downward moving particles causes the observed separation of the mean accelerations of the populations. (*b*) Vertical particle acceleration distributions at different friction velocities. The symmetric distributions widen as the friction velocity increases.

Figure 9(*a*) displays profiles of mean vertical acceleration. A negative acceleration of order g is found for both upward moving and downward moving particles, confirming that the vertical motion of the saltators is approximately ballistic. The upward moving particles, however, experience measurably larger accelerations. This is due to the vertical component of the drag force acting in opposite direction for both populations. Moreover, the magnitude of the downward acceleration for the ensemble of all particles is measurably smaller than g, suggesting the presence of a sizable upward lift force. These considerations will be quantified in the next subsection. The PDF in figure 9(*b*) indicates that the vertical acceleration variance also increases with friction velocity, and even more markedly than for the horizontal component.

3.2. *Force analysis and reconstruction of wind velocity*

The measurement of the accelerations allows us to solve the particle equation of motion instantaneously for each particle. As a result, the fluid velocity can be inferred close to the sand bed, where it is not accessible with PIV measurements. Nishimura & Hunt (2000) solved such an equation to calculate particle trajectories but did not measure the particle accelerations. Therefore, they could not calculate the lift force (which was assumed to be negligible), and the fluid velocity was assumed to be instantaneously equal to its temporal mean. This assumption likely leads to underestimation of the forces, because saltating particles are well in the nonlinear drag regime in which turbulent fluctuations lead to a net increase of the mean drag (Maxey & Riley 1983; Balachandar & Eaton 2010; Brandt & Coletti 2022).

Here, on the other hand, both lift and drag forces are evaluated, as well as the instantaneous fluid velocity at the particle location. We start from Newton's second law,

$$m\boldsymbol{a} = \boldsymbol{F_D} + \boldsymbol{F_L} + \boldsymbol{F_g}, \tag{3.2}$$

where $m = (1/6)\rho_p \pi d_p^3$ is the particle mass, $\boldsymbol{F_D}$, $\boldsymbol{F_L}$ and $\boldsymbol{F_g} = [0, -mg]$ are the drag, lift and gravity force, respectively. Unsteady forces such as added mass and history term are negligible for the present large ratio between particle density and fluid density (Maxey & Riley 1983; Ling, Parmar & Balachandar 2013; Brandt & Coletti 2024). The drag force, aligned with the relative velocity $\boldsymbol{u_r}$, is calculated as

$$\boldsymbol{F_D} = \frac{1}{2}\rho_f C_D \frac{\pi d^2}{4} u_r \boldsymbol{u_r}, \tag{3.3}$$

where

$$C_D = \frac{24}{Re}(1 + 0.15\, Re^{0.687}),\ Re \leqslant 1000. \tag{3.4}$$

Here $Re = u_r \mathrm{d}\nu^{-1}$, the drag coefficient C_D is estimated via the correlation of Schiller & Nauman (see, Clift *et al.* 2005), and the relative velocity is defined as

$$\boldsymbol{u_r} = \boldsymbol{u_f} - \boldsymbol{u}, \tag{3.5}$$

where both the fluid velocity $\boldsymbol{u_f}$ and the relative velocity $\boldsymbol{u_r}$ are taken at the particle location (Horwitz & Mani 2016). The lift force is perpendicular to the drag force by definition:

$$\boldsymbol{F_L} \cdot \boldsymbol{F_D} = 0. \tag{3.6}$$

As the transport is dictated by the balance of forces in the x and y and z directions, we limit our attention to the in-plane components. Therefore, (3.3)–(3.4) define a system of seven scalar equations in eight unknowns: u_{fx}, u_{fy}, u_{rx}, u_{ry}, F_{Dx}, F_{Dy}, F_{Lx} and F_{Ly}. To close the system, we assume that the instantaneous vertical fluid velocity at the particle location is negligibly small compared with other velocity components, $u_{fy} \approx 0$. This is supported by measurements in particle-laden wall turbulence in suspension (Berk & Coletti 2020; Baker & Coletti 2020) and saltation (Raupach 1991). The resulting system of equations is solved for each particle in each frame, obtaining the forces and the horizontal component of the fluid velocity at the particle location. Beside measurement errors, sources of uncertainties of this approach include: neglecting some polydispersity in the particle size; using of the empirical drag correlation (which, while commonly used in particle-laden turbulence, was derived for uniform steady flows (Brandt & Coletti 2024)); assuming a purely horizontal fluid velocity; and neglecting of the out-of-plane relative velocity. With the exception of the latter (which implies a small underestimation of Re), the others are sources of random uncertainty whose influence is expected to shrink with the large number of samples. Moreover, we note that assuming $F_{Lx} \approx 0$ *in lieu* of $u_{fy} \approx 0$ leads to quantitative similar results, implying that the epistemic uncertainty associated with the approach is indeed minor.

The mean horizontal wind velocity is obtained by ensemble-averaging the instantaneous velocity values from the force analysis within vertical bins, each containing at least 10^4 samples. The reconstructed profiles are plotted in figure 10 for the different friction velocities, and appear to be approximately logarithmic throughout. Previous experimental studies have consistently shown convex wind profiles, i.e. a logarithmic region above the saltation layer (where u^* is usually evaluated) and a reduction of the logarithmic slope approaching the bed (Neuman & Nickling 1994; Bauer *et al.* 2004). As discussed by Bauer *et al.* (2004), such curvature of the velocity profile is likely due to the restricted geometry of wind tunnels imposing artificial constraints to the boundary layer development, especially at high speed and when the Froude number $Fr = U_{in}(gh)^{-0.5} > 20$ (where h is the wind tunnel height), see Owen & Gillette (1985). Here the relatively large wind tunnel

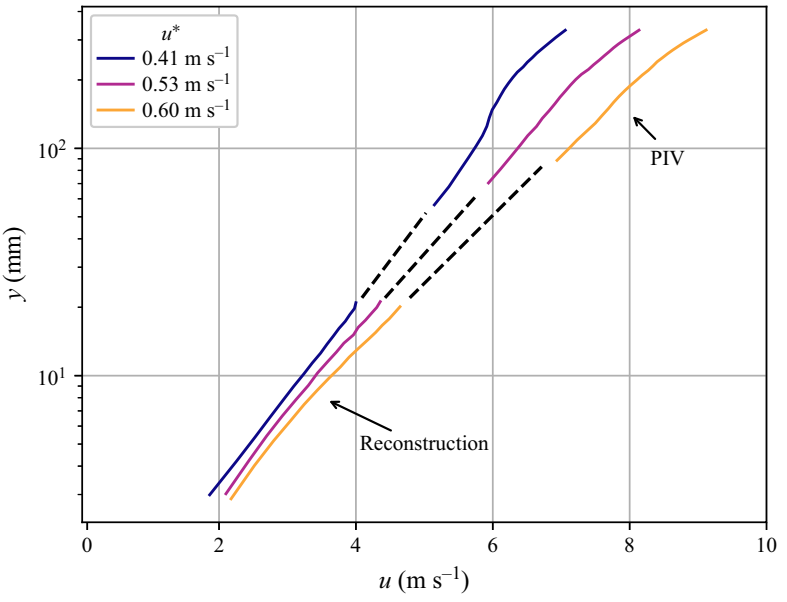

Figure 10. Mean horizontal fluid velocity profile at different friction velocities. The lower part is reconstructed from the particle kinematics, the upper part is measured with PIV. The dashed black lines are linear extrapolations of the reconstructed velocity profiles above 10 mm.

cross-section yields $Fr = 5$–7.8, and indeed a slight curvature of the wind velocity profile is only visible at the higher friction velocities. Moreover, with respect to facilities in which less massive inflow conditioning is applied, the present boundary layer thickness is large with respect to the cross-section dimensions. Therefore, while the conditions are far from those realized in the outdoor environment, the level of geometric confinement of the flow are less severe than in the majority of previous studies.

Besides the approximately constant logarithmic slope, a second remarkable feature of the reconstructed wind velocity profiles is the lack of the so-called Bagnold's focus. In fact, a clear crossing of the wind velocity profiles for different u^* was identified solely in Rasmussen *et al.* (1996), while all later studies measured profiles that only tend to converge (Bauer *et al.* 2004; Rasmussen & Sørensen 2008; Ho *et al.* 2014; O'Brien & Neuman 2019), barely cross (Li & Neuman 2012), or cross at different heights depending on u^* (Ralaiarisoa *et al.* 2020). In figure 10, the logarithmic slope inferred from the velocity reconstruction for $y > 10$ mm (marked by a dashed line) is shown to be fully consistent with the PIV measurements carried out above the saltation layer. This corroborates the validity of the present approach to reconstruct fluid velocity and forces at play, at least in the ensemble-average sense. Only at the higher friction velocity, one can observe some misalignment, which is believed to be the consequence of the above-mentioned slight curvature of the wind profile. Additionally, as PIV and PTV measurements are not carried out simultaneously, minute differences in the experimental conditions may play a role.

For the evaluation of the forces, we ensemble-average equation (3.3). The horizontal direction, assuming the horizontal component of the lift force to be negligible, yields a simple balance between drag and inertia force: $F_{Dx} = ma_x$. The mean horizontal drag force is therefore directly linked to the mean horizontal particle acceleration profiles (figure 8*a*). Accordingly, the drag grows sharply with increasing distance from the bed and plateaus only in the outer region of the saltation layer. Even at the lowest measurement heights (3 mm or $14\,d_p$), the drag force is comparable to gravity ($F_{Dx}\,F_g^{-1} \approx a_x\,g^{-1}$)

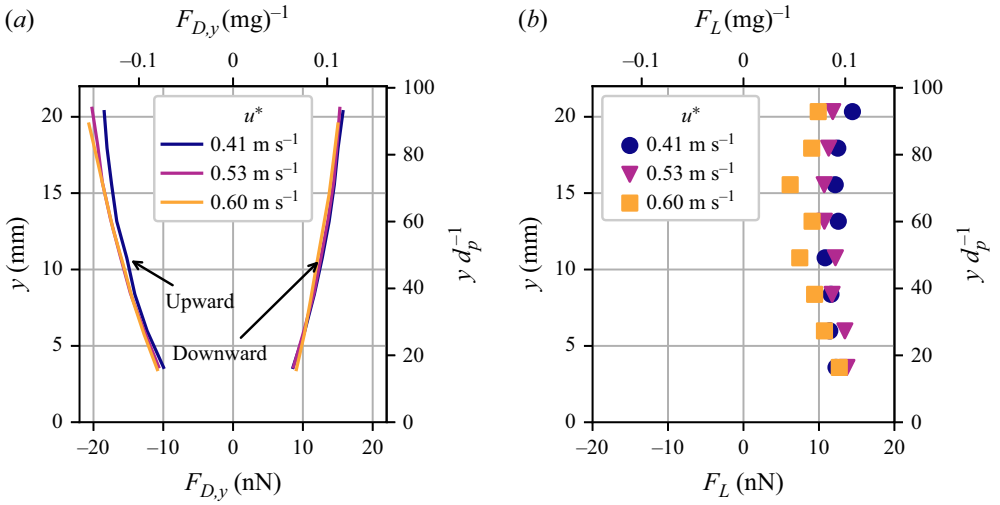

Figure 11. Mean vertical forces acting on the saltating particles. Panel (*a*) shows the mean vertical drag force for different friction velocities. The distribution is mostly symmetric and constant with changes in friction velocity. Panel (*b*) depicts the corresponding lift force. Both forces have the same order of magnitude of $O(0.1\ \mathrm{g})$. The uncertainty on the lift force based on run-to-run variability is 6 %.

and in fact exceeds it for the ejected particles at the higher friction velocities. Drag also acts in positive and negative y direction for the downward and upward moving particles, respectively, with a comparable magnitude of $O(0.1\ F_g)$ and an increasing trend with distance from the bed (figure 11*a*). Figure 11(*b*) shows a sizable lift force, also of magnitude $O(0.1F_g)$, which acts in positive y direction. Despite the experimental scatter, a trend towards lower lift forces at higher friction velocities is visible. Since the Saffman effect is deemed negligible in saltation (Kok *et al.* 2012), the magnitude and trend of the lift force may be due to differences in the rotational particle dynamics and the associated Magnus effect (White & Schulz 1977; Xie, Ling & Zheng 2007; Zou *et al.* 2007; Huang *et al.* 2010). Alternatively, the trend might be associated with increased collision rate (Ralaiarisoa *et al.* 2020) randomizing the rotation rate of the particles and thus reducing the influence of the Magnus effect. These aspects deserve further scrutiny via imaging approaches with higher resolution. Beside such trends, the estimated magnitude of the lift force is consistent with the numerical simulations by Kok & Renno (2009), who verified the Magnus effect as the dominant lift mechanism. Indeed, according to the classic formula by Rubinow & Keller (1961) relating such lift and the particle rotation rate, we estimate the latter to be $O(100\ \mathrm{rpm})$ which is consistent with imaging measurements by Zou *et al.* (2007) in similar conditions. We note that wall-induced lift is negligible in the present range of wall-particle distances (more than 10 particle diameters), see Shi & Rzehak (2020).

3.3. *Reconstruction of saltation trajectory*

The high resolution of the present imaging system, necessary to precisely track the saltating particles, indirectly limits the streamwise extent of the field of view. Along with the spanwise particle motion (O'Brien & Neuman 2018) and the relatively high concentration approaching the bed, this limits the capability of tracking saltating particles over the full hop length. Alternatively, we reconstruct the saltation length by assuming ballistic motion in the vertical direction.

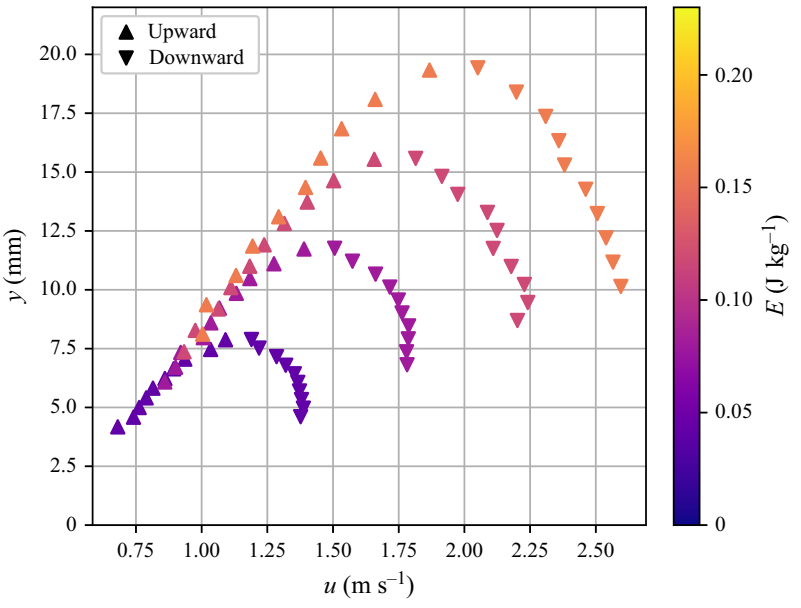

Figure 12. Vertical evolution of mean horizontal particle velocity for different specific vertical energies. The particles accelerate past their apex and eventually reach a terminal velocity, which is characteristic for each energy class.

The hypothesis of ballistic motion in the vertical direction, justified by the observation that vertical drag and lift are relatively small compared with gravity, amounts to assuming that the specific vertical energy $E = 0.5v^2 + gy$ is constant along each trajectory. We indeed verify that E varies by at most 15 % along each trajectory (not shown for brevity). We then split the ensemble of the trajectories into 'energy classes' associated with different values of E, such that the average of the saltation length L can be written as

$$\langle L \rangle = \frac{1}{n} \sum_{n} L = \frac{1}{n} \sum_{E} \sum_{n_E} L = \sum_{E} \frac{n_E}{n} \langle L \rangle_E. \tag{3.7}$$

Here n is the total number of trajectories, n_E is the number of trajectories in an energy class and $\langle \cdot \rangle_E$ represents the average of a given energy class. The saltation length in each energy class is calculated by integrating the horizontal particle velocity,

$$\langle L \rangle_E = \frac{1}{n_E} \sum_{n_E} L = \frac{1}{n_E} \sum_{n_E} \int_{t_0}^{t'} u \, \mathrm{d}t = \int_{t_0}^{t'} \langle u \rangle_E \, \mathrm{d}t, \tag{3.8}$$

where t_0 is the lift-off time and t' is the time at which the particle returns to the bed. This temporal integration can be transformed into a spatial one with the assumption of ballistic motion in the vertical direction,

$$\mathrm{d}y = v \, \mathrm{d}t = \sqrt{2(E - gy)} \, \mathrm{d}t. \tag{3.9}$$

The integration for the upward and downward branches of the trajectory are calculated separately, to obtain an injective mapping from time to height,

$$\langle L \rangle_E = \int_0^{y_A} \frac{\langle u_\uparrow \rangle_E}{\sqrt{2(E - gy)}} \mathrm{d}y - \int_0^{y_A} \frac{\langle u_\downarrow \rangle_E}{\sqrt{2(E - gy)}} \mathrm{d}y, \tag{3.10}$$

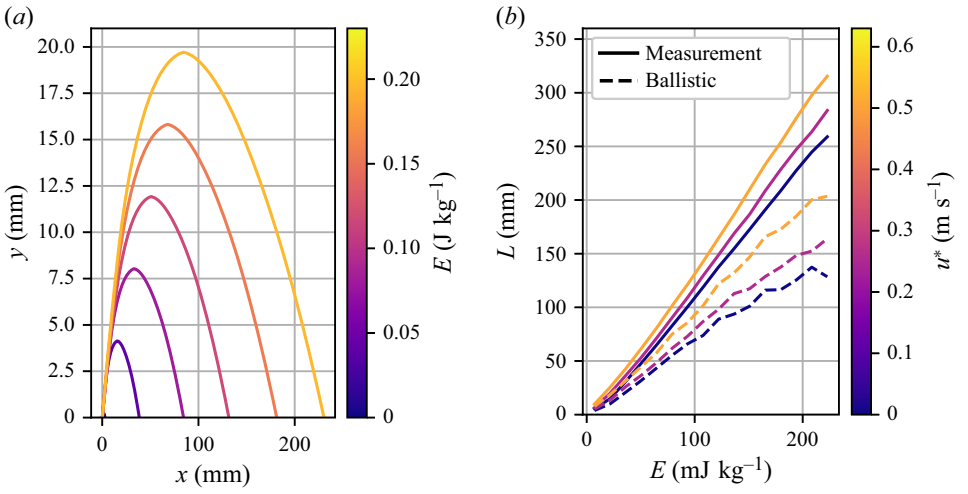

Figure 13. (*a*) Reconstructed average saltation trajectories for different vertical energies. The profiles are not self-similar, but exhibit a skewness, which increases with increasing vertical energy. This increase is due to a combination of increasing drag force and increasing time of flight. (*b*) Average saltation length as a function of specific vertical energy. The dashed lines denote the saltation length in purely ballistic flight, computed from the lift-off velocity. The difference between the measured and the ballistic curves highlight the influence of fluid drag on saltation length.

where $\langle u_{\uparrow} \rangle$ and $\langle u_{\downarrow} \rangle$ are the mean velocity of the upward and downward moving particles, respectively, and $y_A = E\mathrm{g}^{-1}$ is the vertical height of a trajectory apex. This integral is approximated using the measured horizontal velocity profiles, binning the data with respect to the values of E averaged over each particle trajectory. Figure 12 plots, for the representative case at $u^* = 0.41$ m s^{-1}, the resulting relation between height and streamwise velocity for upward and downward moving particles and for different energy classes. Despite the data discretization and the effect of vertical drag and lift (neglected in this analysis), each curve appears to reach an apex close to the theoretical (ballistic) height y_A. Performing this separation unveils the diminishing mean acceleration particles experience along their trajectories.

Integrating these velocity profiles yields the mean trajectory shape for a given specific vertical energy, as plotted in figure 13(*a*), again for the case $u^* = 0.41$ m s^{-1}. The trajectory shapes are not self-similar, with a skewness that increases with E. This is due to the longer time of flight of more energetic particles, during which the horizontal drag plays an increasingly important role. To quantify the effect of drag, figure 13(*b*) displays the corresponding mean saltation length as a function of specific vertical energy at different friction velocities, comparing with the length of purely ballistic trajectories. The latter are obtained using the lift-off velocity, which is estimated by extrapolating the measured vertical velocity to the bed surface. The aerodynamic drag increases the saltation length by more than 50 %.

Having obtained $\langle L \rangle_E$ for different values of E, the mean saltation length can be obtained from the PDF of the specific energy $p(E)$. Rather than performing the integration in the energy E, this is done in the vertical velocity at lift off, $v_0 = \sqrt{2E}$, leveraging the fact that $p(v_0)$ is known to follow a Gaussian form related to the exponential decay of the concentration profile (Creyssels *et al.* 2009; Durán *et al.* 2012; Kang & Zou 2014),

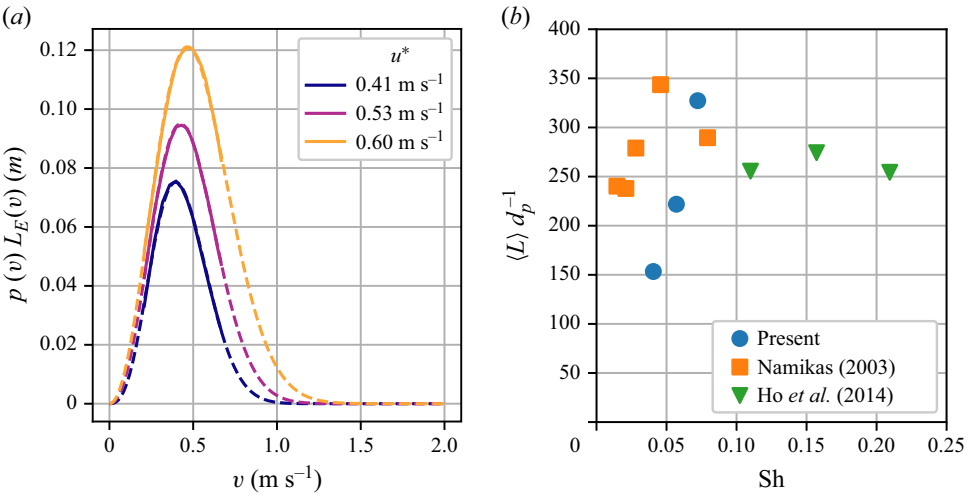

Figure 14. (*a*) Kernel used to compute the mean saltation length for different friction velocities. Dashed lines depict the polynomial extrapolation. (*b*) Mean saltation lengths as a function of Shields number, compared with the wind tunnel data of Ho *et al.* (2014) and the field data of Namikas (2003).

$$p(v_0) = \frac{1}{\sqrt{g h_s \pi}} \exp\left(\frac{-v_0^2}{2 g h_s}\right), \tag{3.11}$$

$$\langle L \rangle = \int_0^\infty p(v_0)\, \langle L \rangle(v_0)\, \mathrm{d}v_0. \tag{3.12}$$

As the data is available in a finite velocity range, we use a fourth-order polynomial to fit the experimentally observed $p(v_0)$, with the constraints $p(0) = 0$ and a zero first derivative at $p(v_0) = 0$, to extrapolate the missing tails. The experimental distributions of $p(v_0)\langle L \rangle_E$ and the analytical fit are shown in figure 14(*a*), while figure 14(*b*) plots the saltation lengths resulting from the integration. Expressed in particle diameters, the values are approximately consistent with previous studies such as the field data by Namikas (2003) and the wind tunnel study by Ho *et al.* (2014). However, we again observe a marked increase with friction velocity, with the mean saltation length roughly doubled in the considered range. In a similar range, Namikas (2003) also showed an increase with *Sh*, though followed by a decrease.

4. Saltation height over a wide range of *Sh*

The previous sections point towards an increasing particle transport with u^* (and therefore with *Sh*) in terms of saltation height, saltation length and particle streamwise velocity. The range of *Sh* over which these trends are measured, however, is limited. To corroborate this observation, we consider the concentration measurements in the second campaign, carried out over a much wider range of *Sh*. Those display again exponential profiles from which we extract the saltation height h_s, plotted in figure 15. The growing trend over two decades of *Sh* is apparent and beyond the experimental uncertainty (estimated from the standard deviation between multiple runs carried out for each *Sh*).

The quantitative comparison with other studies is hampered by various factors mentioned above, including differences in RH, particle properties and boundary layer

properties. The only previous laboratory study that covered a comparable range of Sh is by Ralaiarisoa *et al.* (2020) who also found an increasing h_s with Sh, but only above a critical level $Sh \approx 0.3$. Supported by numerical simulation, they argued that this was due to the transition from the classic saltation regime of quasiballistic trajectories to a regime in which midair collisions are prevalent. They reported the characteristic decay height of mass flux profiles, which cannot be directly compared with the saltation height measured here. The importance and influence of midair collisions was highlighted also in numerical and theoretical studies, e.g. Carneiro *et al.* (2013) and Pähtz & Durán (2020). One may hypothesize that midair collisions are also responsible, at least in part, for the presently observed increasing saltation height (and in general, increasing transport) with Sh. Compared with previous studies in which this effect might have been significant only at relatively large Sh, our experiments are carried out at larger Re_τ, which implies a broader range of turbulent scales. Those may act to enhance the relative interparticle velocities and collision probability, in particular due to extreme fluid velocity fluctuations (Bec, Gustavsson & Mehlig 2024). This may explain why we observe an increasing trend of h_s over the entire range of considered Sh, unlike Ralaiarisoa *et al.* (2020) who used a wind tunnel with a 27 cm by 27 cm cross-section. To confirm such a view, midair collisions would have to be captured simultaneous to the local air flow, which, however, is not presently feasible. Interestingly, the present results appear to indicate three distinct trends: the saltation height increases up to $Sh < 0.1$, remains approximately constant for intermediate Sh, and then increases further when Sh exceeds unity. This seem consistent with the theoretical modelling by Berzi, Jenkins & Valance (2016) who found a succession of three transport regimes with increasing Shields number: one just above the motion threshold, which is not limited by the splash; a splash-limited regime, for which the mass flux increases linearly with the friction velocity and the saltation height is constant; and a collisional transport regime where interparticle collisions contribute to sustain the mass loading. This view implies that impact is the dominant entrainment mechanism only in the intermediate regime, while aerodynamic entrainment and collisions play significant roles in the first and third regime, respectively. This would explain the dependence of the saltation properties on the friction velocity (as well as the lack of Bagnold's focus) in our results in § 3.2. Further studies are warranted to verify this picture and to confirm the precise boundaries of the three regimes.

5. Discussion

We have carried out a laboratory study of aeolian saltation, whose distinguishing features include: the use of size-selected spherical particles; the relatively thick boundary layer; the high spatiotemporal resolution of the measurements. Let us discuss these three features, along with their implications.

First, the present glass microspheres are much more regular in shape and their size distribution is much narrower compared with natural occurring sand, such as commonly used quartz grains (e.g. Neuman & Nickling 1994; Rasmussen *et al.* 1996; Bauer *et al.* 2004; Li & Neuman 2012). While spherical particles do not represent natural properties of aeolian settings, they allow us to reduce the influence of uncontrolled factors, such as the particle self-sorting during saltation. For example, O'Brien & Neuman (2019) found the median diameter of quartz sand in the near-bed region of the saltation cloud to increase markedly with friction velocity. Comola & Lehning (2017) found that ejections of heterogeneous sand are far more frequent than for uniform sand, increasing the separation between fluid threshold and impact threshold. Moreover, the non-spherical shape of natural particles may significantly affect the inception wind speed, collision dynamics, rotation rate and aerodynamic drag (Wang, Ren & Huang 2014; Dun *et al.* 2018; Chen *et al.* 2019).

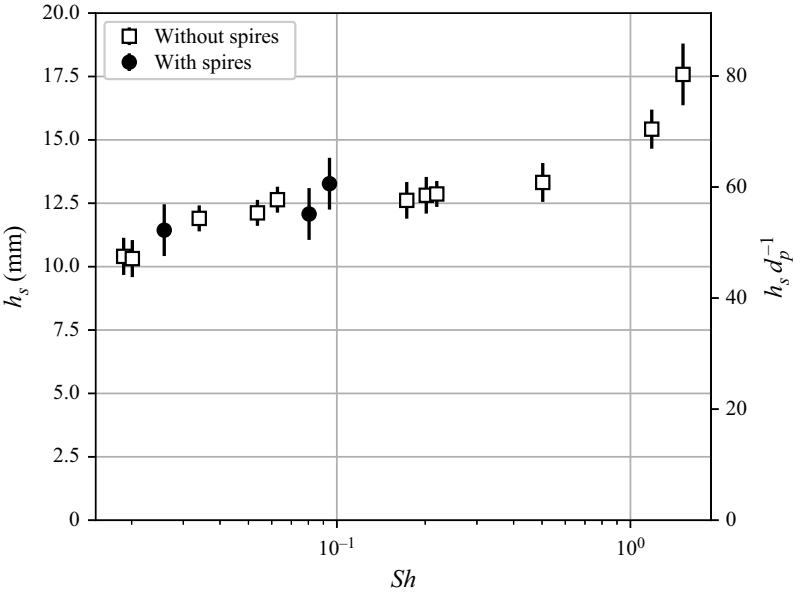

Figure 15. Saltation decay height at different Shields numbers. The error bars are estimated from the standard deviation between multiple runs at each Shields number.

Second, the relatively thick boundary layer compared with most previous laboratory studies is enabled by the dimensions of the tunnel and by the extensive use of inflow conditioning to promote its growth. We stressed in the Introduction (§ 1) how the geometric confinement complicates the evaluation of u^* and artificially modifies the velocity profile, producing changes in the logarithmic slope above the saltation layer (Bauer *et al.* 2004). At the high Re_τ relevant to aeolian saltation, the logarithmic layer is confined to the region $y\delta^{-1} < 0.12$ (Chauhan, Nagib & Monkewitz 2007; Marusic *et al.* 2010), thus a typical saltation height $h_s \approx 50\, d_p$ or 10 mm for the considered particles (Ho *et al.* 2012) would be contained in it only if $\delta > 90$ mm. In fact, as saltating particles reach well above the conventional height h_s obtained from the exponential decay of the particle concentration, δ should be much larger still for the saltation process to be fully embedded within the logarithmic layer. Moreover, δ controls the range of amplitudes and time scales of the turbulent wind velocity fluctuations (Pähtz *et al.* 2018), whose importance in aeolian saltation has been increasingly appreciated in recent years. Using particle-resolved simulations, Lee & Balachandar (2012) and Li *et al.* (2020) showed the effect of turbulence on the hydrodynamic forces and critical shear stress determining incipient motion. The experiments by Hout (2013) highlighted the relation between saltating particle trajectories and near-wall turbulence structures. The large-eddy simulations of Zheng, Jin & Wang (2020) stressed the importance of large-scale turbulent eddies, leading to sand transport by aerodynamic entrainment below the impact threshold. The numerical simulations of Hu, Johnson & Meneveau (2023) emphasized the importance of small-scale turbulent fluctuations in the resuspension of particles lifted from a bed with multiscale asperities. Li *et al.* (2020) experimentally quantified the impact of turbulent fluctuation on the excursions of surface shear stresses and thus on fluid entrainment. Turbulent fluctuations are also key ingredients for interparticle collisions (Bec *et al.* 2024), which in turn crucially affect the transport (Pähtz & Durán 2020). Overall, considering the enormous range of scales accommodated by the atmospheric surface layer and the specific features of wall

turbulence emerging at high Reynolds numbers (such as very large-scale motions and extreme stress fluctuations, see Smits, McKeon & Marusic (2011) and Liu & Zheng (2021)), the conditions $\delta \gg h_s$ and $Re_\tau \geqslant O(10^4)$ appear necessary to reproducing the aeolian dynamics. Only a few of the previous studies reported the boundary layer thickness, but this can be estimated to be comparable to the cross-section half-height. This implies that the maximum Re_τ attained in studies such as Creyssels *et al.* (2009) and Ho *et al.* (2011) are an order of magnitude lower compared with the present experiments.

Third, the present imaging system enables the acquisition of novel and extensive data. Besides providing more detailed profiles of concentration and velocities with respect to previous studies, the use of high-speed time-resolved imaging and the implementation of Lagrangian particle tracking results in higher accuracies compared with non-time resolved strategies (Schröder & Schanz 2023). Crucially, it has enabled the first measurements of particle accelerations in the saltation layer. This has allowed us to verify the applicability and limitation of the key assumption of ballistic vertical motion, to reconstruct the fluid velocity at the particle location and to evaluate the forces acting on the particles.

The dynamic model based on the particle equation of motion allows us to infer the mean wind velocity down to 3 mm from the bed. The agreement with the PIV measurements above the saltation layer lends credibility to the present approach. To our knowledge, only the laser-Doppler anemometry study of Li & Neuman (2012) reported airflow velocities this close to the bed in saturated saltation. Those authors described the challenges associated with performing laser-Doppler anemometry in those conditions, specifically in discriminating between saltating particles and flow tracers, which forced them to consider particles of diameter $d_p = 550\,\mu\text{m}$, twice as large as in the present study. Further studies are warranted to investigate the flow profiles at similar or even smaller distances from the bed with alternative techniques.

The approach we follow allows us to evaluate the saltation length, which is an important quantity to determine the mass transport. The alternative of evaluating it directly from Lagrangian trajectories is necessarily limited to wind speeds relatively close to the transport threshold, in order to limit particle concentration and avoid optical occlusion (Zhang, Kang & Lee 2007). Approaches conceptually similar to the present one were followed by Creyssels *et al.* (2009) and Ho *et al.* (2014). In those studies, experiments were used to define the particle velocity distribution at the bed, which, however, could only be determined at several particle diameters from it, whereas we utilize the measurement of the full velocity profile. The trend of the inferred saltation length is consistent with the one of the saltation height, which is directly observed through the concentration profile and the trajectory apexes.

6. Conclusions

With the above in mind, we summarize our findings in the bullet points below.

(i) In terms of particle concentration. The vertical profiles clearly follow an exponential shape, with a characteristic height of the saltation layer that increases substantially with friction velocity, as shown by measurements spanning two decades of *Sh*.

(ii) In terms of particle mean velocity. The profiles exhibit a convex shape, are sensitive to the friction velocity in the considered range and suggest that also the relative velocity of the particles at the bed is dependent on it.

(iii) In terms of particle acceleration. The distributions of horizontal accelerations are positively skewed, though they contain negative tails associated with particles

travelling faster than the fluid. The vertical accelerations indicate that gravity dominates, though separating upward and downward moving particles highlights the effect of vertical drag and lift forces.

(iv) In terms of air flow velocity. The mean wind velocity profiles, reconstructed down to millimetric distances from the bed and consistent with PIV measurements farther in the boundary layer, have an approximately constant logarithmic slope, increase with increasing friction velocity and do not show a focus.

(v) In terms of forces acting on the particles. The aerodynamic drag force increases with distance from the wall and, for the upward moving particles, exceeds the gravity force already at distances $O(10\,d_p)$ from the bed. The vertical drag component resists the motion of both upward and downward moving particles with a magnitude $\approx 0.1\,F_g$, which is comparable to the lift force. The latter decreases somewhat with increasing friction velocity, possibly because of differences in the rotational effect of the collision dynamics, which, however, could not be resolved with the present measurements.

(vi) In terms of particle trajectories. Coupling the assumption of ballistic vertical motion and the measured streamwise velocities, the mean trajectories are found to be strongly influenced by aerodynamic drag, resulting in saltation heights and lengths that increase with the friction velocity. The direct identification of trajectory apexes also confirms the increase of saltation height with Sh.

Taken together, those results indicate that aerodynamic effects, in particular the aerodynamic drag and lift forces, may play a more significant role in the saltation process than presently recognized. On one side the influence of the wind forcing on the key transport properties is apparent; on the other, the aerodynamic drag and lift forces have significant magnitudes across the entire saltation layer. Therefore, the present results may support the interpretation by Walter *et al.* (2014) that splash and aerodynamic effects are complementary rather than alternative processes. Moreover, the intense air turbulence and its broad range of scales may induce frequent midair collisions, boosting the height and length of saltation and in general increasing the transport.

The findings clearly indicate that common assumptions (in particular those prescribing saltation properties independent of the friction velocity at full transport capacity) need further scrutiny. The discrepancy with previous studies could be rooted in processes that might be differently represented in different experimental and/or numerical set-ups, such as particle polydispersity or the range of scales in the turbulent boundary layer and midair interparticle collisions. Finally, processes that we could not address here, such as granular electrification and electrostatic effects in general, may increase collision rates and provide a significant force in the downward direction (Kok & Renno 2008; Ruan, Gorman & Ni 2024).

While we have focused on steady saltation, it would be interesting to leverage the present facility and measurement approach to investigate intermittent saltation, as the latter is highly sensitive to large-scale velocity fluctuations (Paterna, Crivelli & Lehning 2016). Moreover, further research is warranted to address via Lagrangian measurements the similarity and differences between the considered processes and the transport (Melo *et al.* 2024).

Funding. We gratefully acknowledge funding from the ERC consolidator grant EXPAT (REF-1131-52105) funded by the Swiss State Secretariat for Education, Research and Innovation

Declaration of interests. The authors report no conflict of interest.

References

Ancey, C. & Pascal, I. 2020 Estimating mean bedload transport rates and their uncertainty. *J. Geophys. Res. Earth Surf.* **125**, e2020JF005534.

Andreotti, B., Claudin, P. & Pouliquen, O. 2006 Aeolian sand ripples: experimental study of fully developed states. *Phys. Rev. Lett.* **96**, 028001.

Bagnold, R.A. 1938 The measurement of sand storms. *Proc. R. Soc. Lond. A: Math. Phys. Sci.* **167** (929), 282–291.

Bagnold, R.A. 1941 *Bagnold41*. Chapman and Hall/Methuen.

Baker, L.J. & Coletti, F. 2020 Particle-fluid-wall interaction of inertial spherical particles in a turbulent boundary layer. *J. Fluid Mech.* **908**, A39.

Balachandar, S. & Eaton, J.K. 2010 Turbulent dispersed multiphase flow. *Annu. Rev. Fluid Mech.* **42** (1), 111–133.

Bauer, B.O., Houser, C.A. & Nickling, W.G. 2004 Analysis of velocity profile measurements from wind-tunnel experiments with saltation. *Geomorphology* **59**, 81–98.

Bec, J., Gustavsson, K. & Mehlig, B. 2024 Statistical models for the dynamics of heavy particles in turbulence. *Annu. Rev. Fluid Mech.* **41**, 36.

Beladjine, D., Ammi, M., Oger, L. & Valance, A. 2007 Collision process between an incident bead and a three-dimensional granular packing. *Phys. Rev. E* **75**, 061305.

Berk, T. & Coletti, F. 2020 Transport of inertial particles in high-Reynolds-number turbulent boundary layers. *J. Fluid Mech.* **903**, A18.

Berk, T. & Coletti, F. 2021 Dynamics of small heavy particles in homogeneous turbulence: a Lagrangian experimental study. *J. Fluid Mech.* **917**, A47.

Berzi, D., Jenkins, J.T. & Valance, A. 2016 Periodic saltation over hydrodynamically rough beds: aeolian to aquatic. *J. Fluid Mech.* **786**, 190–209.

Besnard, J.-B., Dupont, P., El Moctar, A.O. & Valance, A. 2022 Aeolian erosion thresholds for cohesive sand. *J. Geophys. Res. Earth Surf.* **127**, e2022JF006803.

Brandt, L. & Coletti, F. 2022 Particle-laden turbulence: progress and perspectives. *Annu. Rev. Fluid Mech.* **54** (1), 159–189.

Brandt, L. & Coletti, F. 2024 Particle-laden turbulence: progress and Perspectives. *Annu. Rev. Fluid Mech.* **44**, 51.

Capecelatro, J. 2022 Modeling high-speed gas–particle flows relevant to spacecraft landings. *Intl J. Multiphase Flow* **150**, 104008.

Carneiro, M.V., Araújo, N.A.M., Pähtz, T. & Herrmann, H.J. 2013 Midair collisions enhance saltation. *Phys. Rev. Lett.* **111**, 058001.

Chauhan, K.A., Nagib, H.M. & Monkewitz, P.A. 2007 *On the Composite Logarithmic Profile in Zero Pressure Gradient Turbulent Boundary Layers*, vol. 9. American Institute of Aeronautics and Astronautics Inc.

Chen, Y., Zhang, J., Huang, N. & Xu, B. 2019 An experimental study on splash functions of natural sand-bed collision. *J. Geophys. Res.: Atmospheres* **124**, 7226–7235.

Claudin, P., Charru, F. & Andreotti, B. 2011 Transport relaxation time and length scales in turbulent suspensions. *J. Fluid Mech.* **671**, 491–506.

Clauser, F.H. 1956 The turbulent boundary layer. *Adv. Appl. Mech.* **4**, 1–51.

Clift, R., Grace, J.R. & Weber, M.E. 2005 *Bubbles, Drops, and Particles*, p. 111. Dover Edition.

Clifton, A., Rüedi, J.D. & Lehning, M. 2006 Snow saltation threshold measurements in a drifting-snow wind tunnel. *J. Glaciol.* **52**, 585–596.

Comola, F. & Lehning, M. 2017 Energy- and momentum-conserving model of splash entrainment in sand and snow saltation. *Geophys. Res. Lett.* **44**, 1601–1609.

Creyssels, M., Dupont, P., Moctar, A.O.E., Valance, A., Cantat, I., Jenkins, J.T., Pasini, J.M. & Rasmussen, K.R. 2009 Saltating particles in a turbulent boundary layer: experiment and theory. *J. Fluid Mech.* **625**, 47–74.

Dong, Z., Qian, G., Luo, W. & H., Wang. 2006 Analysis of the mass flux profiles of an aeolian saltating cloud. *J. Geophys. Res. Atmos.* **111**, D16111.

Doorschot, J.J.J. & Lehning, M. 2002 Equilibrium saltation: mass fluxes, aerodynamic entrainment, and dependence on grain properties. *Boundary-Layer Meteorol.* **104**, 111–130.

Dun, H., Huang, N., Zhang, J. & He, W. 2018 Effects of shape and rotation of sand particles in saltation. *J. Geophys. Res.: Atmos.* **123**, 13462–13471.

Durán, O., Andreotti, B. & Claudin, P. 2012 Numerical Simulation of Turbulent Sediment Transport, From Bed Load to Saltation. *Phys. Fluids* **24**.

FONG, K.O., AMILI, O. & COLETTI, F. 2019 Velocity and spatial distribution of inertial particles in a turbulent channel flow. *J. Fluid Mech.* **872**, 367–406.
HASSAINI, R. & COLETTI, F. 2022 Scale-to-scale turbulence modification by small settling particles. *J. Fluid Mech.* **949**, A30.
HASSAINI, R., PETERSEN, A.J. & COLETTI, F. 2023 Effect of two-way coupling on clustering and settling of heavy particles in homogeneous turbulence. *J. Fluid Mech.* **976**, A12.
HO, T.D., DUPONT, P., MOCTAR, A.OULD EL & VALANCE, A. 2012 Particle velocity distribution in saltation transport. *Phys. Rev. E* **85**, 052301.
HO, T.D., VALANCE, A., DUPONT, P. & MOCTAR, A.O.E. 2011 Scaling laws in aeolian sand transport. *Phys. Rev. Lett.* **106**, 094501.
HO, T.D., VALANCE, A., DUPONT, P. & MOCTAR, A.O.E. 2014 Aeolian sand transport: length and height distributions of saltation trajectories. *Aeolian Res.* **12**, 65–74.
HORWITZ, J.A.K. & MANI, A. 2016 Accurate calculation of Stokes drag for point–particle tracking in two-way coupled flows. *J. Comput. Phys.* **318**, 85–109.
HOUT, R.V. 2013 Spatially and temporally resolved measurements of bead resuspension and saltation in a turbulent water channel flow. *J. Fluid Mech.* **715**, 389–423.
HU, R., JOHNSON, P.L. & MENEVEAU, C. 2023 Modeling the resuspension of small inertial particles in turbulent flow over a fractal-like multiscale rough surface. *Phys. Rev. Fluids* **8**, 024304.
HUANG, N., WANG, C. & PAN, X. 2010 Simulation of aeolian sand saltation with rotational motion. *J. Geophys. Res. Atmos.* **115**, D22211.
KANG, L. & ZOU, X. 2014 Theoretical analysis of particle number density in steady aeolian saltation. *Geomorphology* **204**, 542–552.
KOK, J.F., PARTELI, E.J.R., MICHAELS, T.I. & KARAM, D.B. 2012 The physics of wind-blown sand and dust. *Rep. Prog. Phys.* **75**, 106901.
KOK, J.F. & RENNO, N.O. 2008 Electrostatics in wind-blown sand. *Phys. Rev. Lett.* **100**, 014501.
KOK, J.F. & RENNO, N.O. 2009 A comprehensive numerical model of steady state saltation (COMSALT). *J. Geophys. Res. Atmos.* **114**, D17204.
LEE, H. & BALACHANDAR, S. 2012 Critical shear stress for incipient motion of a particle on a rough bed. *J. Geophys. Res. Earth Surf.* **117**, F01026.
LI, B. & NEUMAN, C.M. 2012 Boundary-layer turbulence characteristics during aeolian saltation. *Geophys. Res. Lett.* **39**, L11402.
LI, G., ZHANG, J., HERRMANN, H.J., SHAO, Y. & HUANG, N. 2020 Study of aerodynamic grain entrainment in aeolian transport. *Geophys. Res. Lett.* **47** (11), e2019GL086574.
LING, Y., PARMAR, M. & BALACHANDAR, S. 2013 A scaling analysis of added-mass and history forces and their coupling in dispersed multiphase flows. *Intl J. Multiphase Flow* **57**, 102–114.
LIU, H. & ZHENG, X. 2021 Large-scale structures of wall-bounded turbulence in single- and two-phase flows: advancing understanding of the atmospheric surface layer during sandstorms. *Flow* **1**, E5.
LIU, X. & DONG, Z. 2004 Experimental investigation of the concentration profile of a blowing sand cloud. *Geomorphology* **60**, 371–381.
MARTIN, R.L. & KOK, J.F. 2017 Wind-invariant saltation heights imply linear scaling of aeolian saltation flux with shear stress. *Sci. Adv.* **3** (6), e1602569.
MARTIN, R.L. & KOK, J.F. 2018 Distinct thresholds for the initiation and cessation of aeolian saltation from field measurements. *J. Geophys. Res.: Earth Surf.* **123**, 1546–1565.
MARUSIC, I., MCKEON, B.J., MONKEWITZ, P.A., NAGIB, H.M., SMITS, A.J. & SREENIVASAN, K.R. 2010 Wall-bounded turbulent flows at high Reynolds numbers: Recent advances and key issues. *Phys. Fluids* **22**, 1–24.
MAXEY, M.R. & RILEY, J.J. 1983 Equation of motion for a small rigid sphere in a nonuniform flow. *Phys. Fluids* **26**, 883–889.
MCKENNA NEUMAN, C. & SANDERSON, S. 2008 Humidity control of particle emissions in aeolian systems. *J. Geophys. Res. Earth Surf.* **113**, F02S14.
MELO, D.B., SHARMA, V., COMOLA, F., SIGMUND, A. & LEHNING, M. 2022 Modeling snow saltation: the effect of grain size and interparticle cohesion. *J. Geophys. Res.: Atmos.* **127** (1), e2021JD035260.
MELO, D.B., SIGMUND, A. & LEHNING, M. 2024 Understanding snow saltation parameterizations: lessons from theory, experiments and numerical simulations. *The Cryosphere* **18** (3), 1287–1313.
MORDANT, N., LÉVÊQUE, E. & PINTON, J.F. 2004 Experimental and numerical study of the lagrangian dynamics of high Reynolds turbulence. *New J. Phys.* **6**, 1–44.
NALPANIS, P., HUNT, J.C.R. & BARRETT, C.F. 1993 Saltating particles over flat beds. *J. Fluid Mech.* **251**, 661–685.

NAMIKAS, S.L. 2003 Field measurement and numerical modelling of aeolian mass flux distributions on a sandy beach. *Sedimentology* **50**, 303–326.
NEUMAN, C.M. & NICKLING, W.G. 1994 Momentum extraction with saltation: implications for experimental evaluation of wind profile parameters. *Boundary-Layer Meteorol.* **68** (1), 35–50.
NICKLING, W.G. & NEUMAN, C.M. 2009 *Aeolian Sediment Transport*. Springer Netherlands.
NISHIMURA, K. & HUNT, J.C.R. 2000 Saltation and incipient suspension above a flat particle bed below a turbulent boundary layer. *J. Fluid Mech.* **417**, 77–102.
O'BRIEN, P. & NEUMAN, C.M. 2018 An experimental study of the dynamics of saltation within a three-dimensional framework. *Aeolian Res.* **31**, 62–71.
O'BRIEN, P. & NEUMAN, C.M. 2019 Experimental validation of the near-bed particle-borne stress profile in aeolian transport systems. *J. Geophys. Res.: Earth Surf.* **124**, 2463–2474.
OUELLETTE, N.T., XU, H. & BODENSCHATZ, E. 2006 A quantitative study of three-dimensional lagrangian particle tracking algorithms. *Exp. Fluids* **40**, 301–313.
OWEN, P.R. 1964 Saltation of uniform grains in air. *J. Fluid Mech.* **20**, 225–242.
OWEN, P.R. & GILLETTE, D. 1985 Wind tunnel constraint on saltation. In *Proc. Intl Workshop on the Physics of Blown Sand*, vol. 253–270, pp. 225–242. University of Aarhus.
PATERNA, E., CRIVELLI, P. & LEHNING, M. 2016 Decoupling of mass flux and turbulent wind fluctuations in drifting snow. *Geophys. Res. Lett.* **43** (9), 4441–4447.
PETERSEN, A.J., BAKER, L. & COLETTI, F. 2019 Experimental study of inertial particles clustering and settling in homogeneous turbulence. *J. Fluid Mech.* **864**, 925–970.
PÄHTZ, T., CLARK, A.H., VALYRAKIS, M. & DURÁN, O. 2020 The physics of sediment transport initiation, cessation, and entrainment across aeolian and fluvial environments. *Rev. Geophys.* **58**, e2019RG000679.
PÄHTZ, T. & DURÁN, O. 2017 Fluid forces or impacts: what governs the entrainment of soil particles in sediment transport mediated by a newtonian fluid? *Phys. Rev. Fluids* **2**, 074303.
PÄHTZ, T. & O., DURÁN 2020 Unification of aeolian and fluvial sediment transport rate from granular physics. *Phys. Rev. Lett.* **124**, 168001.
PÄHTZ, T., VALYRAKIS, M., ZHAO, X.H. & LI, Z.S. 2018 The critical role of the boundary layer thickness for the initiation of aeolian sediment transport. *Geosciences (Switzerland)* **8** (9), 314.
RALAIARISOA, J.L., BESNARD, J.B., FURIERI, B., DUPONT, P., MOCTAR, A.O.E., NAAIM-BOUVET, F. & VALANCE, A. 2020 Transition from saltation to collisional regime in windblown sand. *Phys. Rev. Lett.* **124**, 198501.
RASMUSSEN, K.R., IVERSEN, J.D. & RAUTAHEMIO, P. 1996 Saltation and wind-flow interaction in a variable slope wind tunnel. *Geomorphology* **17**, 19–28.
RASMUSSEN, K.R. & SØRENSEN, M. 2008 Vertical variation of particle speed and flux density in aeolian saltation: measurement and modeling. *J. Geophys. Res. Earth Surf.* **113**, F02S12.
RASMUSSEN, K.R., VALANCE, A. & MERRISON, J. 2015 Laboratory studies of aeolian sediment transport processes on planetary surfaces. *Geomorphology* **244**, 74–94.
RAUPACH, M.R. 1991 Saltation layers, vegetation canopies and roughness lengths. In *Aeolian Grain Transport*, (ed. Barndorff-Nielsen, O.E. & Willetts, B.B.), vol. 1, pp. 83–96. Springer Vienna.
RICHTER, D. & GILL, T. 2018 *Challenges and Opportunities in Atmospheric Dust Emission, Chemistry and Transport*, vol. **99**. American Meteorological Society,
RUAN, X., GORMAN, M.T. & NI, R. 2024 Effects of electrostatic interaction on clustering and collision of bidispersed inertial particles in homogeneous and isotropic turbulence. *J. Fluid Mech.* **980**, A29.
RUBINOW, S.I. & KELLER, JOSEPH B. 1961 The transverse force on a spinning sphere moving in a viscous fluid. *J. Fluid Mech.* **11** (3), 447–459.
SALMON, H.R.S., BAKER, L.J., KOZAREK, J.L. & COLETTI, F. 2023 Effect of shape and size on the transport of floating particles on the free surface in a natural stream. *Water Resour. Res.* **59**, e2023WR035716.
SATO, T., KOSUGI, K. & SATO, A. 2004 Development of saltation layer of drifting snow. *Ann. Glaciol.* **38**, 35–38.
SCHRÖDER, A. & SCHANZ, D. 2023 3D Lagrangian particle tracking in fluid mechanics. *Annu. Rev. Fluid Mech.* **55** (1), 511–540.
SHI, P. & RZEHAK, R. 2020 Lift forces on solid spherical particles in wall-bounded flows. *Chem. Engng Sci.* **211**, 115264.
SMITS, A.J., MCKEON, B.J. & MARUSIC, I. 2011 High-Reynolds number wall turbulence. *Annu. Rev. Fluid Mech.* **43**, 353–375.
VALANCE, A., RASMUSSEN, K.R., MOCTAR, A.O.E. & DUPONT, P. 2015 The physics of aeolian sand transport. *C. R. Phys. Granular Phys. / Physique des Milieux Granulaires* **16** (1), 105–117.
VOTH, G.A., PORTA, A.L., CRAWFORD, A.M., ALEXANDER, J. & BODENSCHATZ, E. 2002 Measurement of particle accelerations in fully developed turbulence. *J. Fluid Mech.* **469**, 121–160.

VOWINCKEL, B. 2021 Incorporating grain-scale processes in macroscopic sediment transport models: a review and perspectives for environmental and geophysical applications. *Acta Mech.* **232**, 2023–2050.

WALTER, B., HORENDER, S., VOEGELI, C. & LEHNING, M. 2014 Experimental assessment of Owen's second hypothesis on surface shear stress induced by a fluid during sediment saltation. *Geophys. Res. Lett.* **41**, 6298–6305.

WANG, Z., REN, S., HUANG, N. & MAGAR, V. 2014 Saltation of non-spherical sand particles. *PLoS ONE* **9** (8), e105208.

WEI, T., SCHMIDT, R. & MCMURTRY, P. 2005 Comment on the Clauser chart method for determining the friction velocity. *Exp. Fluids* **38**, 695–699.

WHITE, B.R. & SCHULZ, J.C. 1977 Magnus effect in saltation. *J. Fluid Mech.* **81**, 497–512.

XIE, L., LING, Y. & ZHENG, X. 2007 Laboratory measurement of saltating sand particles' angular velocities and simulation of its effect on saltation trajectory. *J. Geophys. Res. Atmos.* **112**, D12116.

ZHANG, W., KANG, J.-H. & LEE, S.-J. 2007 Tracking of saltating sand trajectories over a flat surface embedded in an atmospheric boundary layer. *Geomorphology* **86**, 320–331.

ZHANG, W., WANG, Y. & LEE, S.J. 2008 Simultaneous PIV and PTV measurements of wind and sand particle velocities. *Exp. Fluids* **45**, 241–256.

ZHENG, X. 2009 *Mechanics of Wind-blown Sand Movements*. Springer.

ZHENG, X., JIN, T. & WANG, P. 2020 The influence of surface stress fluctuation on saltation sand transport around threshold. *J. Geophys. Res. Earth Surf.* **125**, e2019JF005246.

ZOU, X.-Y., CHENG, H., ZHANG, C.-L. & ZHAO, Y.-Z. 2007 Effects of the Magnus and Saffman forces on the saltation trajectories of sand grain. *Geomorphology* **90**, 11–22.